

Article

Properties of Mechanochemically Synthesized Famatinite Cu_3SbS_4 Nanocrystals

Erika Dutková ^{1,*} , Jaroslav Kováč ², Jaroslav Kováč, Jr. ² , Jiří Hejtmánek ³, Petr Levinský ³, Adelia Kashimbetova ⁴, María Jesús Sayagués ⁵, Martin Fabián ¹, Zdenka Lukáčová Bujňáková ¹ , Matej Baláž ¹ , Katarína Gáborová ¹, Viktor Puchý ⁶  and Ladislav Čelko ⁴

¹ Institute of Geotechnics, Slovak Academy of Sciences, Watsonova 45, 040 01 Košice, Slovakia

² Institute of Electronics and Photonics, Slovak University of Technology, Ilkovičová 3, 812 19 Bratislava, Slovakia

³ FZU—Institute of Physics of the Czech Academy of Sciences, Cukrovarnická 10/112, 162 00 Prague, Czech Republic

⁴ Central European Institute of Technology, Brno University of Technology, Purkynova 123, 612 00 Brno, Czech Republic

⁵ Institute of Material Science of Seville (CSIC-US), Américo Vespucio 49, 41092 Seville, Spain

⁶ Institute of Materials Research, Slovak Academy of Sciences, Watsonova 47, 040 01 Košice, Slovakia

* Correspondence: dutkova@saske.sk; Tel.: +421-55-7922606

Abstract: In this study, we report the optoelectric and thermoelectric properties of famatinite Cu_3SbS_4 that was mechanochemically synthesized in a planetary mill from powder elements for 120 min in an inert atmosphere. The tetragonal famatinite Cu_3SbS_4 was nanocrystalline with a crystallite size of 14 nm, as endorsed by Rietveld refinement. High-resolution transmission electron microscopy showed several crystallites in the range of 20–50 nm. Raman spectroscopy proved the purity of the synthesized famatinite Cu_3SbS_4 and chemical-state characterization performed by X-ray photoelectron spectroscopy confirmed that the prepared sample was pure. The Cu^{1+} , Sb^{5+} , and S^{2-} oxidation states in Cu_3SbS_4 sample were approved. The morphology characterization showed homogeneity of the prepared sample. The photoresponse of Cu_3SbS_4 was confirmed from I–V measurements in the dark and under illumination. The photocurrent increase reached 20% compared to the current in the dark at a voltage of 5 V. The achieved results confirm that synthesized famatinite Cu_3SbS_4 can be applied as a suitable absorbent material in solar cells. The performed thermoelectric measurements revealed a figure of merit ZT of 0.05 at 600 K.

Keywords: mechanochemistry; famatinite Cu_3SbS_4 ; nanocrystals; optoelectric properties; thermoelectric properties



Citation: Dutková, E.; Kováč, J.; Kováč, J., Jr.; Hejtmánek, J.; Levinský, P.; Kashimbetova, A.; Sayagués, M.J.; Fabián, M.; Lukáčová Bujňáková, Z.; Baláž, M.; et al. Properties of Mechanochemically Synthesized Famatinite Cu_3SbS_4 Nanocrystals. *Micro* **2023**, *3*, 458–470. <https://doi.org/10.3390/micro3020030>

Academic Editor: Ajit Roy

Received: 8 February 2023

Revised: 10 March 2023

Accepted: 6 April 2023

Published: 13 April 2023



Copyright: © 2023 by the authors. Licensee MDPI, Basel, Switzerland. This article is an open access article distributed under the terms and conditions of the Creative Commons Attribution (CC BY) license (<https://creativecommons.org/licenses/by/4.0/>).

1. Introduction

Ternary semiconductor nanostructures have attracted considerable interest in recent years, owing to their potential applications in the field of optoelectronic devices, photosensitivity, and thermoelectrics [1,2]. Ternary copper–antimony–sulphide materials have gained favor in solar-cell investigations as alternative absorbers because of the fact that they are composed of low-toxicity and Earth-abundant elements [3,4]. Their thermoelectric properties are also interesting [5,6].

Famatinite Cu_3SbS_4 belongs the group of semiconductors that have been extensively investigated recently. Cu_3SbS_4 is a promising p-type semiconductor with a direct band gap of 0.9–1.8 eV, depending on the crystal structure, and a high absorption coefficient of 10^4 – 10^5 cm^{-1} [7]. This material can be used in several applications, namely for solar photo-voltaics [8] and as an advanced electrode for supercapacitor [9], as well as in thermoelectric devices [10].

There are many synthetic approaches for famatinite Cu_3SbS_4 preparation: from compounds [11], from compounds and elements [12], or only from elements [13–18]. Flower-like

Cu_3SbS_4 particles were prepared easily and rapidly from mixtures of CuCl_2 , SbCl_3 , and thiourea in ethylene glycol by microwave radiation [11]. One-pot synthesis of Cu_3SbS_4 nanocrystals by a surfactant-assisted solvothermal method was reported in [12]. Lee et al. [13] synthesized Cu_3SbS_4 by mechanical alloying from pure elements copper, antimony, and sulfur, followed by consolidation using hot pressing. Ge-doped Cu_3SbS_4 was synthesized from pure elements by mechanical alloying combined with spark plasma sintering (SPS) by Chen et al. [14]. High thermoelectric performance in Sn-doped Cu_3SbS_4 prepared from pure elements by a combination of mechanical alloying and spark plasma sintering was also investigated by Chen et al. [15]. Cu_3SbS_4 as thermoelectric material and the enhancement of its figure of merit (ZT) by chemical substitutions was reported in the paper by Suzumura et al. [16]. Chen et al. prepared $\text{Cu}_3\text{Sb}_{1-x}\text{Sn}_x\text{S}_4$ samples from pure elements by mechanical alloying connected with spark plasma sintering in paper [17]. Thermoelectric properties and the thermal stability of Bi- and Sn-doped Cu_3SbS_4 samples were investigated in the paper by Shen et al. [18].

In this connection, high-energy milling utilizing tools of mechanochemistry for the synthesis of nanomaterials also has a place [19]. Additionally, ball milling offers a timesaving alternative to conventional methods [20] and has been successfully applied in the synthesis of nanomaterials. This environmentally friendly route has been already applied for famatinite Cu_3SbS_4 prepared by mechanochemical synthesis in the laboratory and industrial mill, as reported by our research group in a previous paper [21]. The present contribution is a study of the optoelectric properties of nanocrystalline famatinite synthesized via mechanochemistry in a planetary mill. Moreover, the Cu_3SbS_4 powder was consolidated by spark plasma sintering and its suitability for thermoelectrics applications was examined.

2. Materials and Methods

Cu_3SbS_4 nanocrystals were synthesized using 2.16 g of copper (99.7%, Merck, Darmstadt, Germany), 1.38 g of antimony (99.8%, Merck, Darmstadt, Germany), and 1.46 g of sulfur (99%, Itecs, Vranov n/T, Slovakia) in a Cu:Sb:S stoichiometric ratio 3:1:4 according to Equation (1).



The mechanochemical synthesis was performed in a planetary ball mill Pulverisette 6 (Fritsch, Idar-Oberstein, Germany) in an argon atmosphere for only 120 min. A 250 mL tungsten carbide milling chamber with 50 tungsten carbide balls (360 g), 10 mm in diameter, was used. The milling was carried out at 550 rpm. The ball-to-powder ratio was 72:1. The yield of the sample was 97%.

Phase evolution was followed by X-ray powder diffraction (XRD). The XRD data were collected by D8 Advance diffractometer (Bruker, Bremen, Germany) with a $\text{CuK}\alpha$ radiation source. Data were collected in the range $10\text{--}65^\circ$ 2θ and 0.03° step. The XRD data were further analyzed by Rietveld refinement (Fullprof software [22]), and fitted in the space group I-42m for Cu_3SbS_4 . The XRD line broadening was refined by application of regular Thompson–Cox–Hastings pseudo-Voigt function parameters. The instrumental line broadening was verified by refinement of an LaB_6 standard specimen. The phase identification was performed by utilization of JCPDS PDF [23].

Scanning electron microscopy (SEM), transmission electron microscopy with high-resolution (TEM/HR-TEM) and electron diffraction (ED) techniques were used for the structural and morphological characterization of the sample. A few drops of an acetone dispersion from small amounts of powder sample were deposited on a carbon-coated nickel grid in a case of TEM measurements. The SEM microscope used to perform the morphological analysis was a Hitachi S-4800-FEG with field-emission filament. To carry out the microstructural characterization and analysis composition, a 200 kV JEOL-2100-PLUS microscope (JEOL, Akishima, Japan) with a LaB_6 filament (0.25 nm inter-dot resolution) and equipped with an energy-dispersive X-ray detector (EDX, Oxford Instrument, Nanolab Technologies Inc., Milpitas, CA, USA) was used. High-resolution image analysis and fast Fourier transform (FFT) were performed with a Gatan Digital Micrograph (Gatan Inc., Pleasanton, CA, USA) and JEM software (version

number 3.3806U2009). The INCA program was used to quantify the chemical composition of the sample. The X-ray detector coupled to the microscope have internal standards that allow semi-quantitative analysis, showing an elemental ratio percentage.

Micro-Raman spectra were measured using a confocal Raman microscope (Spectroscopy & Imaging, Warstein, Germany) and a focused Ar laser beam with a wavelength of 514 nm.

Elemental compositions of the samples were evaluated by X-ray photoelectron spectroscopy (XPS; Kratos Axis Supra, Manchester, UK) with monochromatized AlK α radiation ($h\nu = 1486.69$ eV) in the range of 0–1200 eV. The scanning was performed at an emission current of 4 mA using hybrid-lens mode. XPS survey and core-level spectra were recorded using scanning steps of 1.0 and 0.1 eV, respectively. Fitting and peak deconvolution were carried out using the Casa XPS software (Version 2.3.17, Casa Software Ltd., Teignmouth, UK). Prior to the data analysis, the C1s spectrum was calibrated at 284.8 eV. Low-resolution wide-survey spectrum and high-resolution spectra for Cu, Sb, and S were performed. The high-resolution spectra were deconvoluted using a Shirley-type background.

The measurement of zeta-potential (ZP) was carried out using a Zetasizer Nano ZS (Malvern Instruments Ltd., Malvern, UK). The ZP was obtained from the electrophoretic mobility by the Smoluchowski equation. The ZP was measured in the original dispersion medium and the measurements were repeated three times.

Micro PL spectra were obtained in the Vis-NIR region with the same confocal Raman microscope (Spectroscopy & Imaging, Warstein, Germany). To broaden the spectrum in the visible region, excitation at 488 nm was chosen by retuning the Ar laser.

I–V characteristics were measured on prepared devices using an Agilent semiconductor parameter analyzer (4155C). The devices were measured in the dark and under focused halogen lamp illumination. The illumination intensity of the focused beam reached 600 mW/cm². The measured device was prepared by dropping a solution of nanocrystalline powder in isopropyl alcohol onto an interdigital structure with Au contacts. The connection of the interdigital structure to the socket was realized by means of wires glued with silver paste.

In order to allow thermoelectric characterization, the powder was placed into a graphite die (inner diameter 10 mm) and sintered into pellets about 5 mm thick at 723 K under 50 MPa with heating rate of 323 K/min and holding time of 3 min in a spark plasma sintering furnace model HP D10-SD (FCT Systeme GmbH, Frankenblick, Germany) in vacuum.

The pellets were cut for subsequent analyses by a diamond wire saw. The electrical resistivity and Seebeck coefficient were measured under nitrogen flow in a temperature range between 300 and 620 K via the four-probe method using a custom-made instrument. Thermal conductivity was calculated as a product of thermal diffusivity, heat capacity, and density. The first two properties were measured between 200 and 600 K using the Netzsch LFA 467 instrument utilizing Pyroceram 9606 as a standard for heat capacity. Density was determined from the dimensions and mass of the sample and considered temperature-independent.

3. Results

3.1. Structural and Microstructural Characterization

Tetragonal famatinite Cu₃SbS₄ prepared by mechanochemical synthesis after 120 min of milling was proven by XRD. All the diffraction peaks (101), (112), (200), (202), (211), (114), (105), (220), (312), and (224) coincided well with the JCPDS card of tetragonal famatinite (JCPDS-00-066-0317). The famatinite crystallized in the space group I-42m (121) with the lattice parameters $a = b = 5.40146$ Å and $c = 10.70920$ Å, $\alpha = \beta = \gamma = 90^\circ$. No diffraction peaks belonging to other phases in the Cu–Sb–S system were identified in the XRD pattern. The crystallite size determined by Rietveld refinement was ~14 nm. The estimated microstrain was $\epsilon_0 19.8 \times 10^{-4}$ and the goodness parameter χ^2 was 3.85. Amorphization and the formation of small crystallites strongly influenced XRD pattern. TEM/ED/EDS results are presented in Figure 1b. The TEM image shows the nanocrystalline character of the sample. The crystallites were agglomerated into large particles, and the ED rings could be indexed in the famatinite tetragonal (T) structure in good agreement with the XRD results. Although the average crystalline domain shown by XRD was 14 nm, the HR-TEM images showed

several crystallites in the range of 20–50 nm. The HR micrograph presents a crystal oriented along the $[3\ 3\ 1]_{\text{T}}$ zone axis and the corresponding Fast Fourier transform (FFT) is inset. A semiquantitative analysis of the sample was carried out by EDS analysis; small areas (only 2 or 3 crystallites) and larger zones (several microns) were measured, finding a homogenous result, presented in the EDX spectrum showing the average of the atomic ratio percentage: 35/14/51 for Cu/Sb/S, which is quite similar to the stoichiometric formula (37.5/12.5/50).

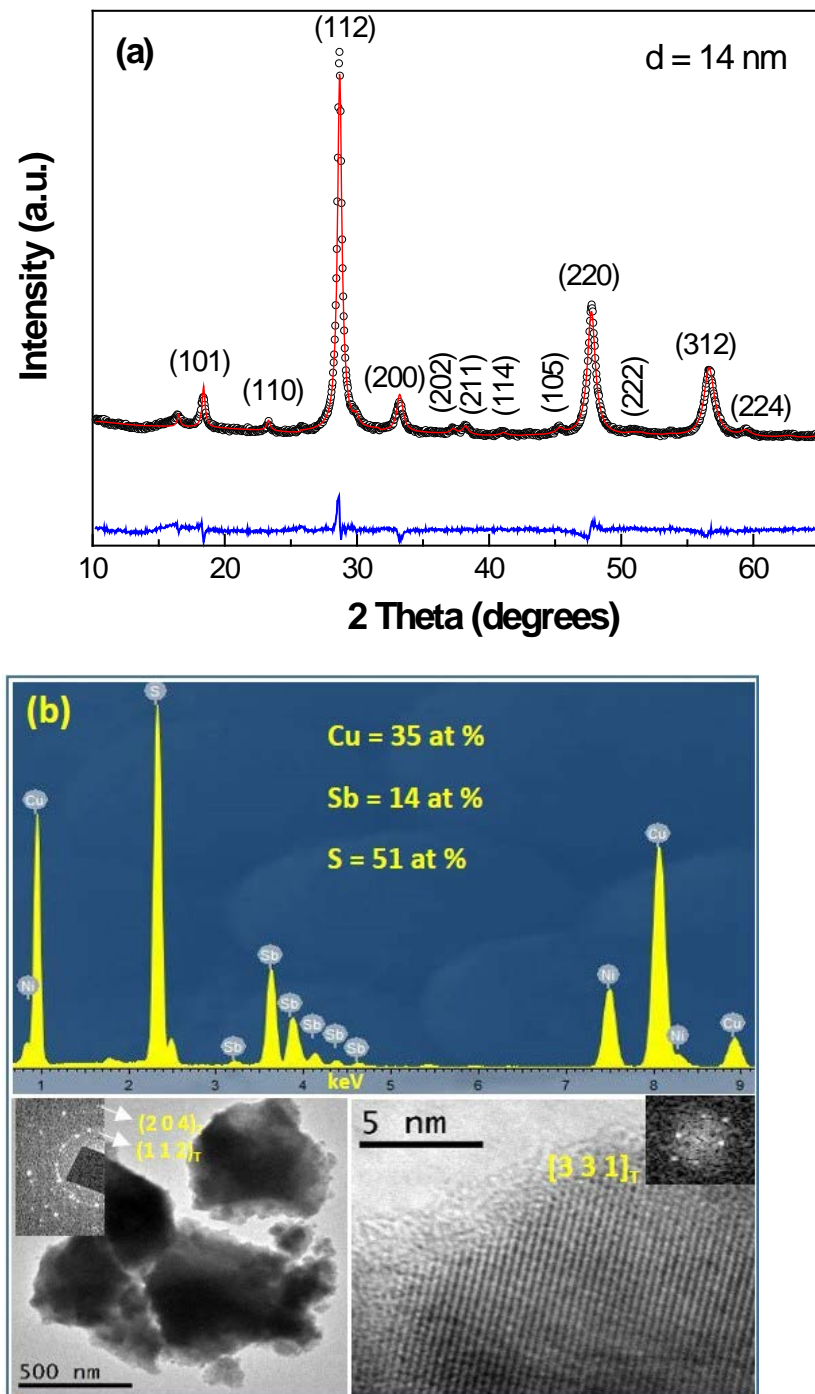


Figure 1. (a) XRD pattern and result of the refinement of mechanochemically synthesized Cu_3SbS_4 . Dots represent measured data, red line shows fitted plot, and blue line represents the difference between observed and model data. (b) HR-TEM results of mechanochemically synthesized Cu_3SbS_4 sample after 120 min of milling.

Micro-Raman spectroscopy with laser excitation of 514 nm was used as an additional tool to analyze the crystallinity and structural phase, and also to distinguish the presence of intermediate phases or impurities. The corresponding micro-Raman spectrum of the synthesized Cu_3SbS_4 nanoparticles after 120 min of milling is shown in Figure 2. The measured spectrum has well distinguishable peaks at 130, 248, 271, 314, and 340 cm^{-1} , which are comparable to the published results described in [24–26] and the RRUFF database for the Cu_3SbS_4 phase. The RRUFF reference spectrum of famatinite Cu_3SbS_4 is included in the inset of Figure 2. The measured micro-Raman spectrum verified the synthesis of phase-pure Cu_3SbS_4 . These results are in good agreement with the XRD measurements and analysis.

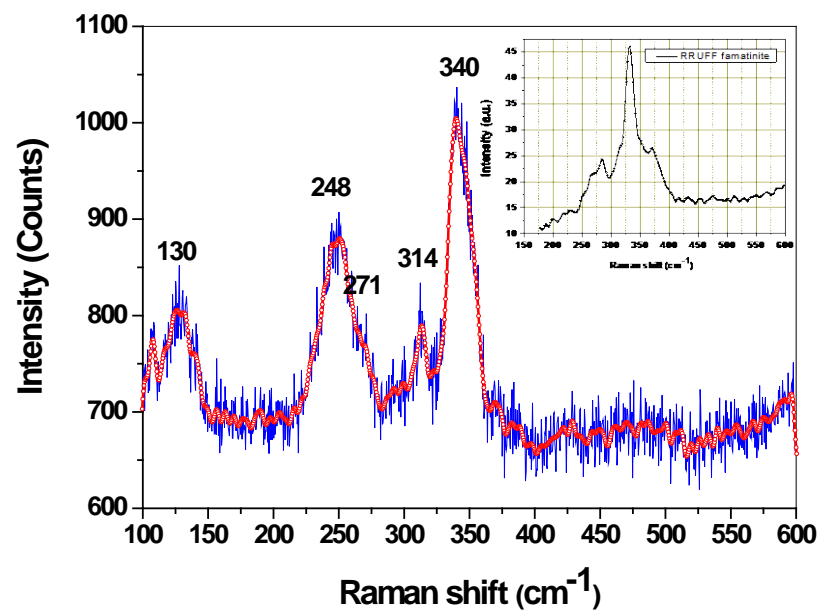


Figure 2. Micro-Raman spectrum of mechanochemically synthesized Cu_3SbS_4 sample after 120 min of milling (blue measured, red smoothed) and RRUFF reference spectrum of famatinite Cu_3SbS_4 (inset).

3.2. Surface Properties

3.2.1. X-ray Photoelectron Spectroscopy (XPS)

X-ray photoelectron spectroscopy (XPS) was applied to elucidate the surface composition of the as-synthesized Cu_3SbS_4 sample. XPS survey and core-level spectra of Cu_3SbS_4 sample prepared after 120 min of milling are shown in Figure 3. The presence of Cu, Sb, and S as well as C from the reference and O impurity was proven by XPS survey spectrum of Cu_3SbS_4 sample (Figure 3a). In order to assign the valency state for the Cu2p, Sb3d, and S2p the core-level spectra were also taken (Figure 3b–d). The Cu2p core-level spectrum is shown in Figure 3b. The core-level spectrum of Cu2p was well-defined and demonstrated the doublet of Cu2p_{3/2} and Cu2p_{1/2} at binding energies of 932.4 and 952.16 eV, respectively, with charge separation ΔE of 19.76 eV which has been adjudged to the Cu^{1+} ion. Moreover, there was no Cu2p_{3/2} satellite peak situated at about 942 eV which is characteristic of Cu^{2+} . The values were consistent with the results reported in paper [11]. Figure 3c is the representative Sb3d core-level spectrum, showing that the Sb3d region had well-separated spin-orbit components observed at 530.37 eV (Sb3d_{5/2}) and 539.69 eV (Sb3d_{3/2}). The Sb3d doublet had separation of 9.32 eV, which is in accordance with the value for Sb^{5+} , as was reported in [11]. Additionally, the Sb3d spectrum of Cu_3SbS_4 had a small signal at 531.70 eV that corresponded to Sb oxides [27]. The S2p core-level spectrum is shown in Figure 3d, where a well-defined doublet of S2p of the sample was observed at 162.20 eV (S2p_{3/2}) and 163.36 eV (S2p_{1/2}), resulting in a separation ΔE of 1.16 eV, which is consistent with sulphur in the sulphide chemical state S^{2-} in the Cu_3SbS_4 . A further peak at a higher binding energy 164.45 eV reflected

some oxidation in the Cu_3SbS_4 sample. However, this observed peak had been previously ascribed to oxidized sulphur species in the form of SO_x , which were located on the surface of the Cu_3SbS_4 sample as was also confirmed by zeta potential value (see below Figure 4). Our results are in accordance with results published in [12]. The formation of Cu_3SbS_4 was confirmed by higher intense peak values of S2p and Sb3d along with value of Cu2p peak in correlation with our XRD results. The confirmed Cu^{1+} , Sb^{5+} , and S^{2-} oxidation states were expected for the Cu_3SbS_4 famatinite sample.

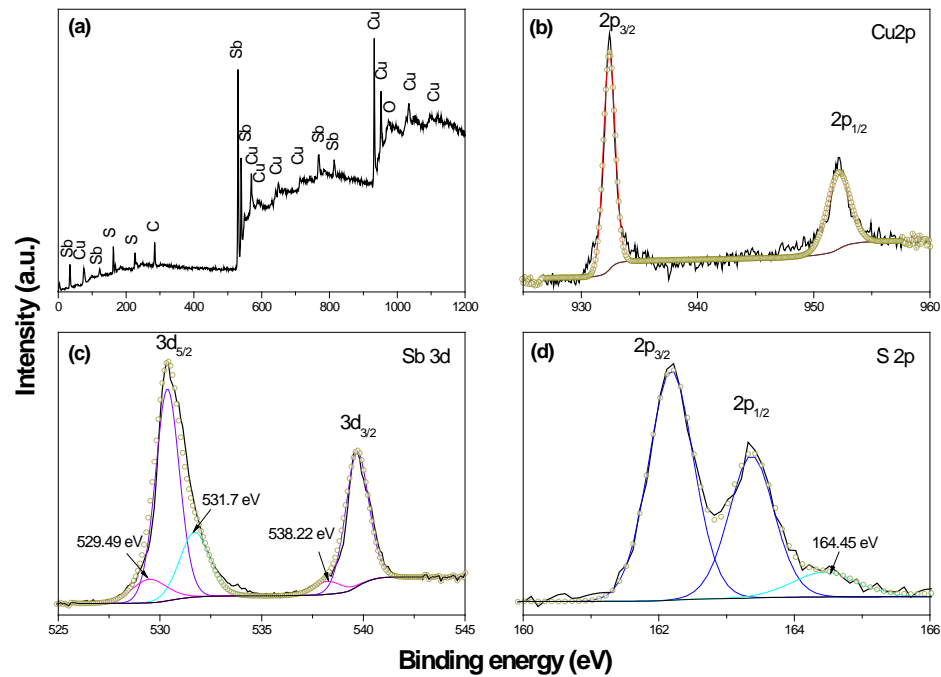


Figure 3. XPS survey spectrum (a) and core-level spectra of: Cu 2p (b), Sb 3d (c), and S 2p (d) for mechanochemically synthesized Cu_3SbS_4 after 120 min of milling.

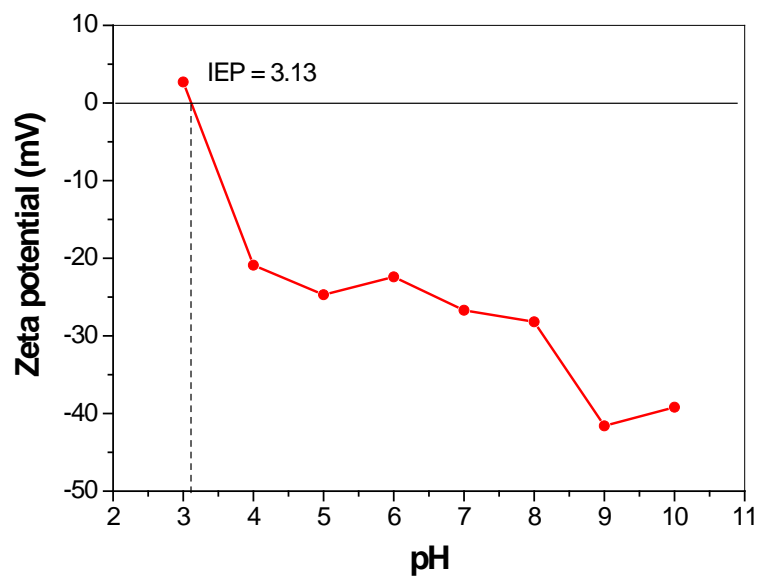


Figure 4. Dependence of zeta potential on the pH of mechanochemically synthesized Cu_3SbS_4 after 120 min of milling.

3.2.2. Zeta Potential

The zeta potential measurement provides appropriate information about the surface properties. The results for the Cu_3SbS_4 sample are displayed in Figure 4. The ZP values were measured in a pH range from 3 to 10. The balance between positive and negative charge on the surface expressed by the isoelectric point (IEP) was observed at pH 3.13. If more alkali was added to the suspension, the particles tended to acquire more negative charge, down to -40.6 mV for pH 9. To the best of our knowledge, the IEP for famatinite has not been reported in the literature. The measured results indicate that the mechanochemically prepared famatinite can be oxidized very slightly on its surface [28,29], as confirmed by XPS analysis (Figure 3d). The slight increase in zeta potential observed above pH 9 may be caused by the compression of the double layer at high ionic strengths [30,31]. The achieved results are in agreement with ones observed for other mechanochemically synthesized sulfides reported in our previous papers [32,33].

3.2.3. Scanning Electron Microscopy (SEM)

SEM was used for the morphology characterization of mechanochemically synthesized famatinite Cu_3SbS_4 after 120 min of milling. A representative SEM image is presented in Figure 5, showing agglomerations of small grains, a typical micrograph of the mechanochemically synthesized sample.

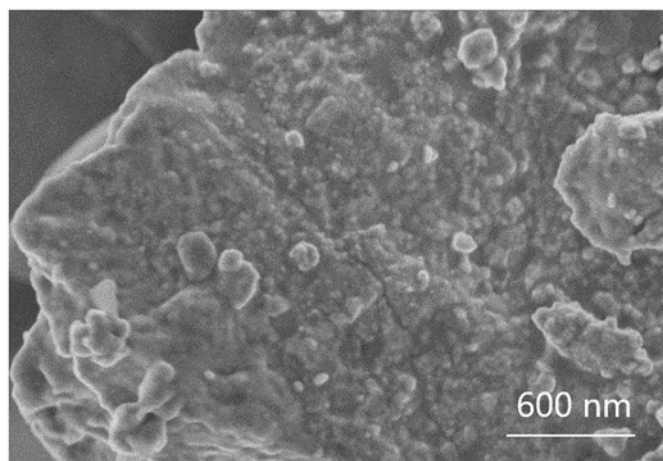


Figure 5. SEM image of mechanochemically synthesized Cu_3SbS_4 after 120 min of milling.

The chemical analysis was also studied by EDS, giving rise to an atomic percentage relationship for Cu/Sb/S (37/14/49) similar to that found by EDS in the TEM microscope. Elemental mapping was taken in several regions to verify the chemical homogeneity through the sample. A representative result is depicted in Figure 6 and shows that the three elements were homogeneously scattered throughout the sample.

3.3. Micro-Photoluminescence Spectroscopy

Nanocrystalline ternary chalcogenide compounds can emit radiation in a wide range of the spectrum, which is determined by the basic luminescence of the semiconductor and, in the case of nanoparticles, by their dimensions and the technology of preparation. In the literature for Cu_3SbS_4 , there are ambiguous data reported about the direct 1.3 eV [7], 1.5 eV [12], and 1.72 eV [34] and indirect 0.82 eV [12] and 1.2 eV [8] band gaps. Figure 7 shows the micro-PL spectrum of mechanochemically synthesized Cu_3SbS_4 under excitation with a wavelength of 488 nm. The measured spectrum was broad with a maximum around 542 nm exhibiting various deflections which indicated the involvement of different luminescence centres in the radiative processes. The fitted peaks in the PL spectra presented in Figure 7 had a maximum determined at 542 nm (2.28 eV) and 688 nm (1.8 eV), indicating

the quantum confinement effect of nanocrystalline Cu_3SbS_4 . These results are comparable to absorption measurements in published results [8] where absorption maxima at 547 and 667 nm were measured for Cu_3SbS_4 nanocrystals. The deflection of the PL spectra with a maximum at 886 nm (1.39 eV) may have been due to the bulk Cu_3SbS_4 emission.

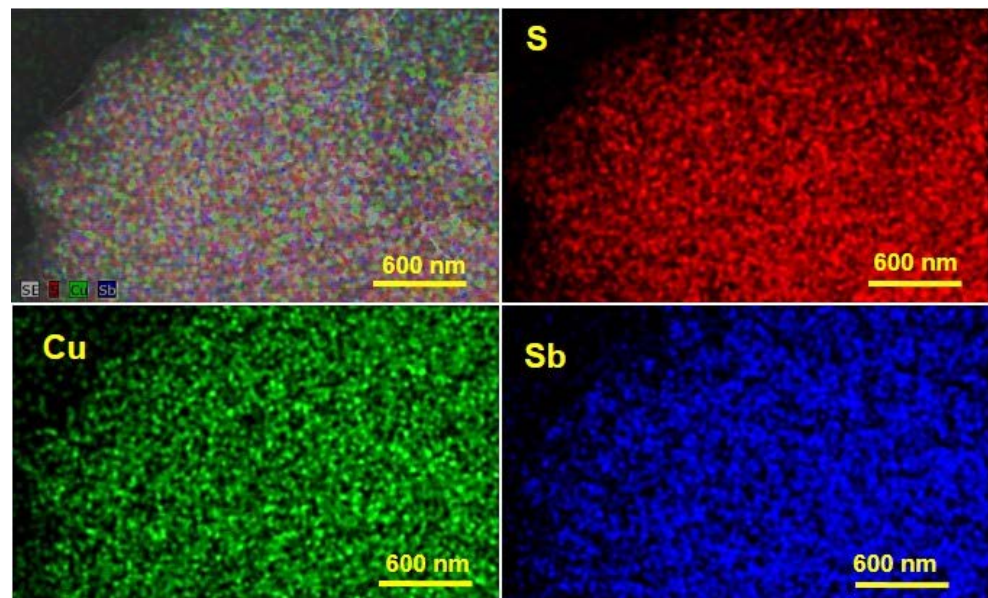


Figure 6. EDS compositional and individual elemental mapping (S, Cu, and Sb) of mechanochemically synthesized Cu_3SbS_4 after 120 min of milling.

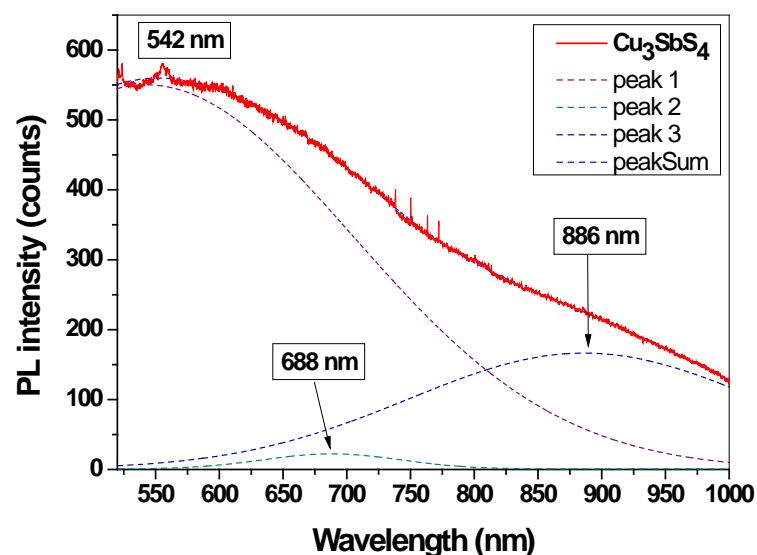


Figure 7. Micro-photoluminescence spectrum of mechanochemically synthesized Cu_3SbS_4 after 120 min of milling excited at 488 nm.

3.4. Optoelectric Measurements

For the analysis of optoelectric properties the I–V characteristics of Cu_3SbS_4 nanoparticles mechanochemically synthesized after 120 min of milling were measured. As shown in Figure 8 the photoresponse of Cu_3SbS_4 was confirmed from I–V measurements in the dark and under illumination. The linear dependence of measured I–V characteristics corresponded to the creation of a sufficient ohmic contact for the measurements. As can be seen in Figure 8, the measured sample showed ~20% increase in photocurrent at 5 V

when illuminated, compared to the current in the dark. The increase in the conductivity of the sample during illumination was due to the increased generation of charge carriers in nanocrystalline Cu_3SbS_4 . The measured results are in good agreement with the I–V measurements given in other works [26,34,35].

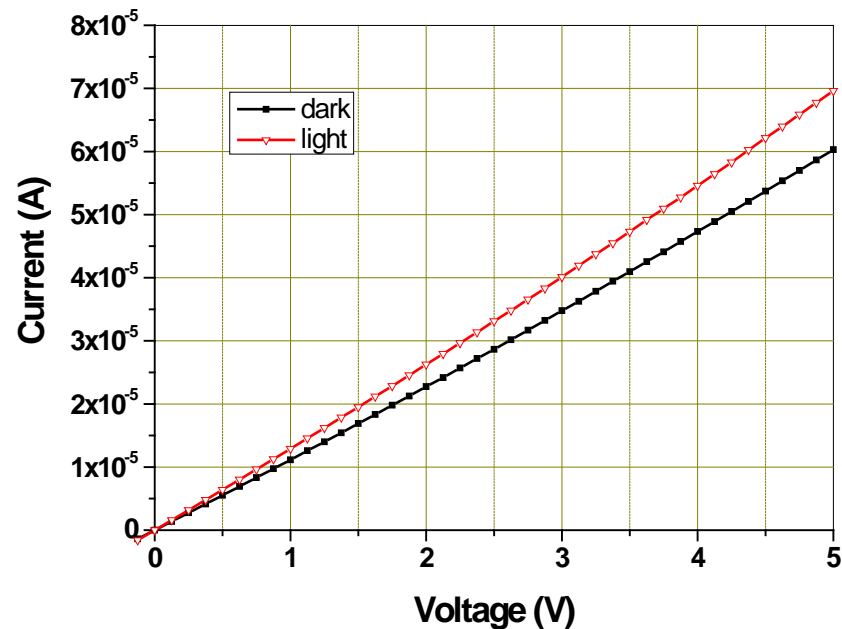


Figure 8. I–V characteristics of Cu_3SbS_4 nanoparticles in the dark and under light illumination.

3.5. Thermoelectric Measurements

Cu_3SbS_4 is known to have moderate thermoelectric performance. Recent studies have shown that ideally doped Cu_3SbS_4 can attain values of the thermoelectric figure of merit $ZT = S^2T/(\rho\kappa)$ between 0.6 and 0.7 at 623 K [14,18,36], where S is the Seebeck coefficient, ρ is the electrical resistivity, and κ is the thermal conductivity. Famatinite possesses fairly high lattice thermal conductivity for a thermoelectric material (about $1\text{--}4 \text{ W}\cdot\text{m}^{-1}\cdot\text{K}^{-1}$ at room temperature), unlike some related materials from the Cu–Sb–S system, such as skinnerite Cu_3SbS_3 or tetrahedrite $\text{Cu}_{12}\text{Sb}_4\text{S}_{13}$ which profit from the presence of lone-pair electrons of the Sb atoms, which help reduce lattice thermal conductivity [37].

Electrical properties (Figure 9) show p-type semiconducting behaviour with electrical resistivity decreasing with temperature and a positive Seebeck coefficient showing a weak temperature dependence and fairly high values. Electrical resistivity (Figure 9a) dropped from $1800 \text{ m}\Omega\cdot\text{cm}$ at room temperature to $400 \text{ m}\Omega\cdot\text{cm}$ at 623 K. The Seebeck coefficient (Figure 9b) reached a value of $600 \mu\text{V}\cdot\text{K}^{-1}$ at 600 K. Similar results were reported in the literature for pristine Cu_3SbS_4 : $585 \mu\text{V}\cdot\text{K}^{-1}$ at 623 K [13] and $580 \mu\text{V}\cdot\text{K}^{-1}$ at 573 K [15], for samples with low carrier concentration ($\sim 10^{17} \text{ cm}^{-3}$ at 300 K), and $\sim 500 \mu\text{V}\cdot\text{K}^{-1}$ at 573 K [16,38], for samples with higher carrier concentration ($\sim 4.2 \times 10^{18} \text{ cm}^{-3}$ at 300 K). Based on these reports we can assume the carrier concentration of our sample to be in the range $10^{17}\text{--}10^{18} \text{ cm}^{-3}$, which is some three orders of magnitude below the optimum concentration attainable by doping [15].

The measured thermal conductivity κ shown in Figure 9c solely reflected the lattice part of κ , as the electronic part was negligible given the high electrical resistivity. As stated above, the absolute value was rather high for a thermoelectric material: $2.1 \text{ W}\cdot\text{m}^{-1}\cdot\text{K}^{-1}$ at room temperature which decreased to the $1.0 \text{ W}\cdot\text{m}^{-1}\cdot\text{K}^{-1}$ at 600 K. This decrease was close to the T^{-1} dependence characteristic of the Umklapp phonon-scattering process. The absolute value was lower than the $1.7 \text{ W}\cdot\text{m}^{-1}\cdot\text{K}^{-1}$ at 573 K reported by Goto et al. [38] for a sample synthesized by solid-state reaction, which can be explained by increased scattering of phonons due to the stronger presence of grain boundaries and defects introduced by

high-energy milling in the nanograined sample. Other studies, however, report even lower values mechanochemically synthesized samples, such as $0.74 \text{ W}\cdot\text{m}^{-1}\cdot\text{K}^{-1}$ at 623 K [13], or $0.7 \text{ W}\cdot\text{m}^{-1}\cdot\text{K}^{-1}$ at 623 K [15]. The principal difference seems to lie in the milling time, which was an order of magnitude longer than the 2 h in our case, thus further amplifying the nanostructuring and defect concentration in the milled product. This suggests that even though 2 h of milling are sufficient for the synthesis of phase-pure powder, further milling has a beneficial effect on the lowering of thermal conductivity of the resulting material.

Since the sample was synthesized as pristine Cu_3SbS_4 , we cannot expect good thermoelectric performance which has to be achieved by doping. Indeed, the maximum of figure of merit ZT reached only 0.05 at 600 K. This value was lower than the 0.14 at 623 K reported in other papers [13,15], where pristine famatinite was synthesized by mechanical alloying, but higher than reported in [16,38] for samples prepared by melting–sintering of elements. Moreover, the lower thermal conductivity of mechanochemically synthesized or mechanically activated samples has an impact on increasing of ZT in contrast to non-milled or non-activated samples [39,40]. Both treatments followed by SPS can be used to prepare ceramics with small grain size [41], where the sources of phonon scattering such as grain boundaries lead to reduced phonon mean free path and, as a consequence, lower lattice thermal conductivity. In the paper [42], it was presented that dry milling of natural tetrahedrite leads to the production of thermoelectrics with increased electrical resistivity, but decreased thermal conductivity, compared to the mineral. This can be attributed to grain size reduction, the role of defects in doping, and grain boundaries in phonon scattering.

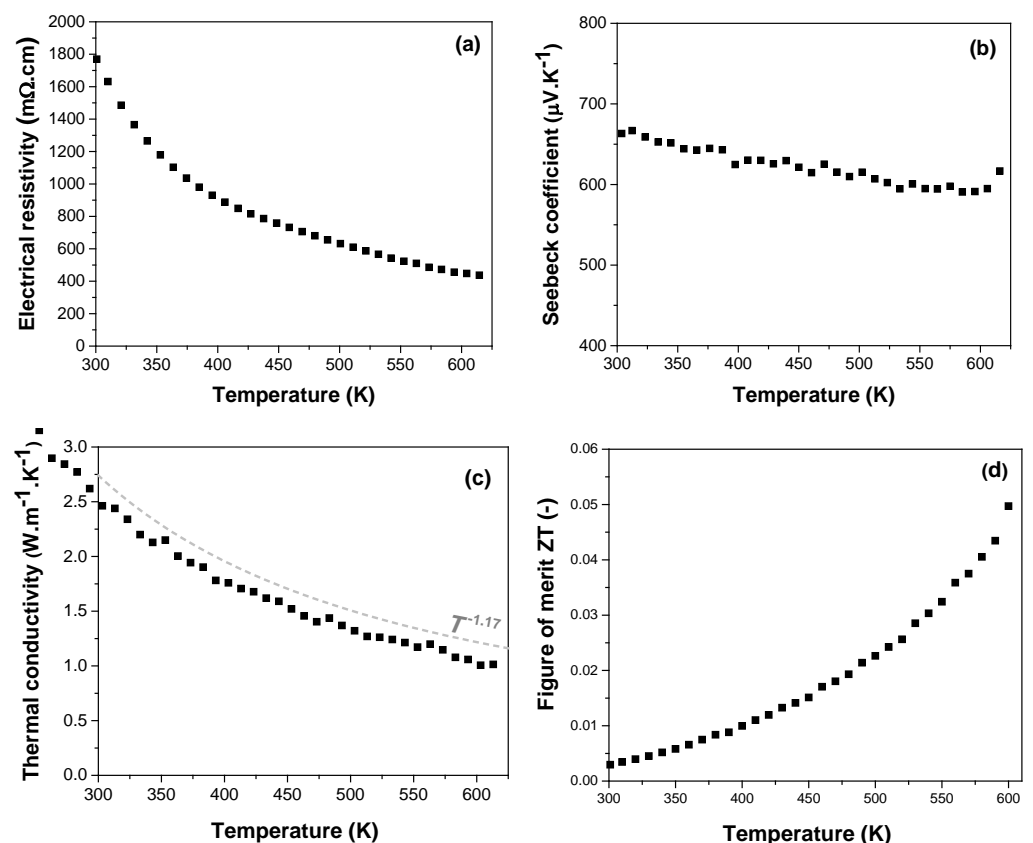


Figure 9. Thermoelectric properties of mechanochemically synthesized Cu_3SbS_4 in dependence of temperature; panels from (a–d) represent electrical resistivity, Seebeck coefficient, thermal conductivity, and figure-of-merit ZT , respectively.

The XRD analysis of famatinite Cu_3SbS_4 after SPS was also performed. For comparison, the XRD patterns of both samples before and after SPS are shown in Figure 10. The very

fine crystallite size resulting in the broad diffraction peaks (Figure 10a) was influenced by the SPS process (Figure 10b), as evidenced by the narrower peaks. An analysis of the XRD spectrum after SPS did not reveal any phases other than famatinite crystallizing in the space group I-42m with the lattice parameters $a = b = 5.39153 \text{ \AA}$ and $c = 10.76360 \text{ \AA}$, $\alpha = \beta = \gamma = 90^\circ$. The crystallite size determined by Rietveld refinement was $\sim 55.8 \text{ nm}$ and the estimated microstrain was $\varepsilon_0 = 4.9 \times 10^{-4}$. These results could be ascribed to enhanced crystallinity and stress release due to sintering in contrast to as-milled famatinite sample before SPS.

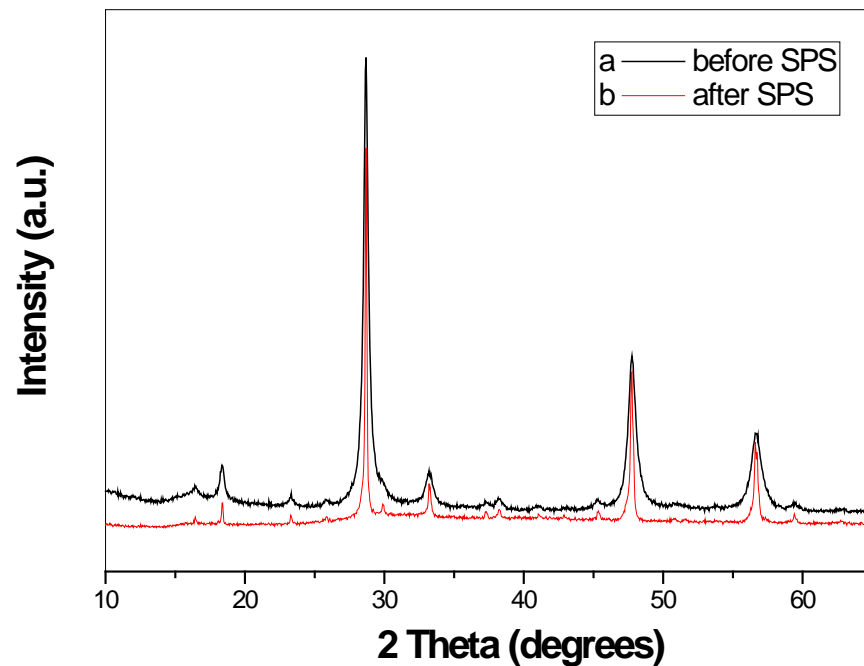


Figure 10. XRD patterns of mechanochemically synthesized famatinite Cu_3SbS_4 (a) before and (b) after SPS.

4. Conclusions

In summary, we studied the properties of famatinite Cu_3SbS_4 nanocrystals mechanochemically synthesized by high-energy milling in a planetary mill in the argon atmosphere at room temperature for 120 min. The crystallite size of the tetragonal famatinite Cu_3SbS_4 determined by Rietveld refinement of XRD data was 14 nm. HR-TEM images showed several crystallites in the range of 20–50 nm, revealing agglomerated nanocrystals and also confirming their tetragonal structure. The zeta potential measurement indicated prepared famatinite Cu_3SbS_4 could be oxidized on its surface very slightly, which was also confirmed by the XPS method. The photoluminescence spectrum indicated the quantum confinement effect of nanocrystalline famatinite Cu_3SbS_4 . The I–V characteristic of the sample with Cu_3SbS_4 nanoparticles showed $\sim 20\%$ increase in photocurrent at 5 V after illumination, which proves that the synthesized tetragonal Cu_3SbS_4 famatinite exhibited the acceptable photoelectric properties and provides a prerequisite for use in photovoltaics. The thermoelectric measurements revealed a figure of merit ZT of 0.05 at 600 K for the undoped famatinite Cu_3SbS_4 sintered by SPS at 723 K. This value could be improved by adjusting the carrier concentration via doping. The prepared famatinite Cu_3SbS_4 represents a prospective material for future applications.

Author Contributions: Conceptualization, E.D.; methodology, J.K., J.K.J., J.H., P.L., A.K., M.J.S., M.F., Z.L.B., K.G. and V.P.; investigation, E.D., J.K., J.K.J., J.H., P.L., A.K., M.J.S., M.F. and Z.L.B.; writing—original draft preparation, E.D.; writing—review and editing, J.K., J.K.J., J.H., P.L., A.K., M.J.S., M.F., Z.L.B., K.G., M.B., V.P. and L.Č. All authors have read and agreed to the published version of the manuscript.

Funding: This study was supported by the Slovak Research and Development Agency (contract No. APVV-18-0357, APVV-20-0437, and 19-0526) and Slovak Grant Agency VEGA (projects 2/0112/22). The support of COST Action CA18112 MechSustInd (www.mechsustind.eu), supported by the COST Association (European Cooperation in Science and Technology, www.cost.eu) is also acknowledged.

Institutional Review Board Statement: Not applicable.

Informed Consent Statement: Not applicable.

Data Availability Statement: The data presented in this study are available on request from the corresponding author.

Acknowledgments: We would like to thank Mariano Casas-Luna for his technical support in XPS analysis.

Conflicts of Interest: The authors declare no conflict of interest. The funders had no role in the design of the study; in the collection, analyses, or interpretation of data; in the writing of the manuscript, or in the decision to publish the results.

References

1. Ghafoor, F.; Ghafoor, B.; Kim, D.; Khan, M.F.; Rehman, M.A. Enhancement in figure of merit in N-type Bi(R)-Te thermoelectric nanomaterials. *J. Mater. Res. Technol.* **2023**, *23*, 3617–3625. [[CrossRef](#)]
2. Pan, Y.; Fan, F.R.; Hong, X.C.; He, B.; Le, C.C.; Schnelle, W.; He, Y.K.; Imasato, K.; Borrmann, H.; Hess, C.; et al. Thermoelectric Properties of Novel Semimetals: A Case Study of YbMnSb₂. *Adv. Mater.* **2021**, *33*, e2003168. [[CrossRef](#)]
3. Tablero, C. Electronic and optical property analysis of the Cu–Sb–S tetrahedrites for high-efficiency absorption devices. *J. Phys. Chem. C* **2014**, *118*, 15122–15127. [[CrossRef](#)]
4. Kehoe, A.B.; Temple, D.J.; Watson, G.W.; Scanlon, D.O. Cu(3)MCh(3) (M = Sb, Bi; Ch = S, Se) as candidate solar cell absorbers: Insights from theory. *Phys. Chem. Chem. Phys.* **2013**, *15*, 15477–15484. [[CrossRef](#)]
5. Powell, A.V. Recent developments in Earth-abundant copper-sulfide thermoelectric materials. *J. Appl. Phys.* **2019**, *126*, 100901. [[CrossRef](#)]
6. Suekuni, K.; Takabatake, T. Research Update: Cu-S based synthetic minerals as efficient thermoelectric materials at medium temperatures. *Appl. Mater.* **2016**, *4*, 104503. [[CrossRef](#)]
7. Kavinchan, J.; Saksornchai, E.; Thongtem, S.; Thongtem, T. One-step microwave assisted synthesis of copper antimony sulphide (Cu₃SbS₄) nanostructures: optical property and formation mechanism study. *Chalcogenide Lett.* **2018**, *15*, 599–604.
8. Ramasamy, K.; Sims, H.; Butler, W.H.; Gupta, A. Selective Nanocrystal Synthesis and Calculated Electronic Structure of All Four Phases of Copper-Antimony-Sulfide. *Chem. Mater.* **2014**, *26*, 2891–2899. [[CrossRef](#)]
9. Mariappan, V.K.; Krishnamoorthy, K.; Pazhamalai, P.; Sahoo, S.; Kim, S.J. Layered famatinite nanoplates as an advanced pseudocapacitive electrode material for supercapacitor applications. *Electrochim. Acta* **2018**, *275*, 110–118. [[CrossRef](#)]
10. Joel van Embden, Y.T. Synthesis and characterisation of famatinite copper antimony sulfide nanocrystals. *J. Mater. Chem.* **2012**, *22*, 11466. [[CrossRef](#)]
11. Chen, G.L.; Wang, W.H.; Zhao, J.F.; Yang, W.Y.; Chen, S.Y.; Huang, Z.G.; Jian, R.K.; Ruan, H.R. Study on the synthesis and formation mechanism of flower-like Cu₃SbS₄ particles via microwave irradiation. *J. Alloys Compd.* **2016**, *679*, 218–224. [[CrossRef](#)]
12. Bella, M.; Rivero, C.; Blayac, S.; Basti, H.; Record, M.C.; Boulet, P. Oleylamine-assisted solvothermal synthesis of copper antimony sulfide nanocrystals: Morphology and phase control. *Mater. Res. Bull.* **2017**, *90*, 188–194. [[CrossRef](#)]
13. Lee, G.E.; Pi, J.H.; Kim, I.H. Preparation and Thermoelectric Properties of Famatinite Cu₃SbS₄. *J. Electron. Mater.* **2020**, *49*, 2781–2788. [[CrossRef](#)]
14. Chen, K.; Du, B.L.; Bonini, N.; Weber, C.; Yan, H.X.; Reece, M.J. Theory-Guided Synthesis of an Eco-Friendly and Low-Cost Copper Based Sulfide Thermoelectric Material. *J. Phys. Chem. C* **2016**, *120*, 27135–27140. [[CrossRef](#)]
15. Chen, K.; Di Paola, C.; Du, B.L.; Zhang, R.Z.; Laricchia, S.; Bonini, N.; Weber, C.; Abrahams, I.; Yan, H.X.; Reece, M. Enhanced thermoelectric performance of Sn-doped Cu₃SbS₄. *J. Mater. Chem. C* **2018**, *6*, 8546–8552. [[CrossRef](#)]
16. Suzumura, A.; Watanabe, M.; Nagasako, N.; Asahi, R. Improvement in Thermoelectric Properties of Se-Free Cu₃SbS₄ Compound. *J. Electron. Mater.* **2014**, *43*, 2356–2361. [[CrossRef](#)]
17. Chen, K.; Di Paola, C.; Laricchia, S.; Reece, M.J.; Weber, C.; McCabe, E.; Abrahams, I.; Bonini, N. Structural and electronic evolution in the Cu₃SbS₄-Cu(3)SnS(4) solid solution. *J. Mater. Chem. C* **2020**, *8*, 11508–11516. [[CrossRef](#)]
18. Shen, M.J.; Lu, S.Y.; Zhang, Z.F.; Liu, H.Y.; Shen, W.X.; Fang, C.; Wang, Q.Q.; Chen, L.C.; Zhang, Y.W.; Jia, X.P. Bi and Sn Co-doping Enhanced Thermoelectric Properties of Cu₃SbS₄ Materials with Excellent Thermal Stability. *ACS Appl. Mater. Inter.* **2020**, *12*, 8271–8279. [[CrossRef](#)]
19. Baláž, P.; Achimovičová, M.; Baláž, M.; Billik, P.; Cherkezova-Zheleva, Z.; Criado, J.M.; Delogu, F.; Dutková, E.; Gaffet, E.; Gotor, F.J.; et al. Hallmarks of mechanochemistry: From nanoparticles to technology. *Chem. Soc. Rev.* **2013**, *42*, 7571–7637. [[CrossRef](#)]
20. James, S.L.; Adams, C.J.; Bolm, C.; Braga, D.; Collier, P.; Friscic, T.; Grepioni, F.; Harris, K.D.M.; Hyett, G.; Jones, W.; et al. Mechanochemistry: Opportunities for new and cleaner synthesis. *Chem. Soc. Rev.* **2012**, *41*, 413–447. [[CrossRef](#)]

21. Dutkova, E.; Sayagues, M.J.; Fabian, M.; Balaz, M.; Achimovicova, M. Mechanochemically synthesized ternary chalcogenide Cu_3SbS_4 powders in a laboratory and an industrial mill. *Mater. Lett.* **2021**, *291*, 129566. [[CrossRef](#)]
22. Rodriguez-Carvajal, J. Recent developments of the program FullProf. Commission on powder diffraction (IUCr). *Newsletter* **2001**, *6*, 12–19.
23. Rodriguez-Carvajal, J.; Roisnel, T. Line broadening analysis using FullProf[®]: Determination of microstructural properties. *Eur. Powder Diffr. Epdic* **2004**, *443–444*, 123–126. [[CrossRef](#)]
24. Chalapathi, U.; Poornaprakash, B.; Park, S.H. Growth and properties of Cu_3SbS_4 thin films prepared by a two-stage process for solar cell applications. *Ceram. Int.* **2017**, *43*, 5229–5235. [[CrossRef](#)]
25. Rahman, A.A.; Hossian, E.; Vaishnav, H.; Parmar, J.B.; Bhattacharya, A.; Sarma, A. Synthesis and characterization of Cu_3SbS_4 thin films grown by co-sputtering metal precursors and subsequent sulfurization. *Mater. Adv.* **2020**, *1*, 3333–3338. [[CrossRef](#)]
26. Han, G.; Lee, J.W.; Kim, J. Fabrication and Characterization of Cu_3SbS_4 Solar Cell with Cd-free Buffer. *J. Korean Phys. Soc.* **2018**, *73*, 1794–1798. [[CrossRef](#)]
27. Shaji, S.; Vinayakumar, V.; Krishnan, B.; Johny, J.; Kanakillam, S.S.; Herrera, J.M.F.; Guzman, S.S.; Avellaneda, D.A.; Rodriguez, G.A.C.; Martinez, J.A.A. Copper antimony sulfide nanoparticles by pulsed laser ablation in liquid and their thin film for photovoltaic application. *Appl. Surf. Sci.* **2019**, *476*, 94–106. [[CrossRef](#)]
28. Fairthorne, G.; Fornasiero, D.; Ralston, J. Interaction of thionocarbamate and thiourea collectors with sulphide minerals: A flotation and adsorption study. *Int. J. Miner. Process.* **1997**, *50*, 227–242. [[CrossRef](#)]
29. Fornasiero, D.; Eijt, V.; Ralston, J. An Electrokinetic Study of Pyrite Oxidation. *Coll. Surf.* **1992**, *62*, 63–73. [[CrossRef](#)]
30. Dukhin, S.S.; Derjaguin, B.V. Non-equilibrium Double Layer and Electrokinetic Phenomena. In *Surface and Colloid Science*; Matijevic, E., Ed.; John Wiley & Sons: New York, NY, USA, 1974; Volume 7, pp. 297–300.
31. Konkena, B.; Vasudevan, S. Understanding Aqueous Dispersibility of Graphene Oxide and Reduced Graphene Oxide through pK(a) Measurements. *J. Phys. Chem. Lett.* **2012**, *3*, 867–872. [[CrossRef](#)]
32. Dutkova, E.; Bujnakova, Z.; Kovac, J.; Skorvanek, I.; Sayagues, M.J.; Zorkovska, A.; Kovac, J.; Balaz, P. Mechanochemical synthesis, structural, magnetic, optical and electrooptical properties of CuFeS_2 nanoparticles. *Adv. Powder Technol.* **2018**, *29*, 1820–1826. [[CrossRef](#)]
33. Dutkova, E.; Sayagues, M.J.; Fabian, M.; Kovac, J.; Kovac, J.; Balaz, M.; Stahorsky, M. Mechanochemical synthesis of ternary chalcogenide chalcostibite CuSbS_2 and its characterization. *J. Mater. Sci.-Mater. El.* **2021**, *32*, 22898–22909. [[CrossRef](#)]
34. Mohamadkhani, F.; Heidariramsheh, M.; Javadpour, S.; Ghavamini, E.; Mahdavi, S.M.; Taghavinia, N. Sb nanocrystals as inorganic hole transporting materials in perovskite solar cells. *Sol. Energy* **2021**, *223*, 106–112. [[CrossRef](#)]
35. Shi, L.; Wu, C.Y.; Li, J.J.; Ding, J. Selective synthesis and photoelectric properties of Cu_3SbS_4 and CuSbS_2 nanocrystals. *J. Alloys Compd.* **2017**, *694*, 132–135. [[CrossRef](#)]
36. Tanishita, T.; Suekuni, K.; Nishiate, H.; Lee, C.H.; Ohtaki, M. A strategy for boosting the thermoelectric performance of famatinite Cu_3SbS_4 . *Phys. Chem. Chem. Phys.* **2020**, *22*, 2081–2086. [[CrossRef](#)]
37. Du, B.L.; Zhang, R.Z.; Chen, K.; Mahajan, A.; Reece, M.J. The impact of lone-pair electrons on the lattice thermal conductivity of the thermoelectric compound CuSbS_2 . *J. Mater. Chem. A* **2017**, *5*, 3249–3259. [[CrossRef](#)]
38. Goto, Y.; Sakai, Y.; Kamihara, Y.; Matoba, M. Effect of Sn-Substitution on Thermoelectric Properties of Copper-Based Sulfide, Famatinite Cu_3SbS_4 . *J. Phys. Soc. Jpn.* **2015**, *84*, 044706. [[CrossRef](#)]
39. Balaz, P.; Dutkova, E.; Levinsky, P.; Daneu, N.; Kubickova, L.; Knizek, K.; Balaz, M.; Navratil, J.; Kasparova, J.; Ksenofontov, V.; et al. Enhanced thermoelectric performance of chalcopyrite nanocomposite via co-milling of synthetic and natural minerals. *Mater. Lett.* **2020**, *275*, 128107. [[CrossRef](#)]
40. Levinsky, P.; Hejtmanek, J.; Knizek, K.; Pashchenko, M.; Navratil, J.; Masschelein, P.; Dutkova, E.; Balaz, P. Nanograined n- and p-Type Chalcopyrite CuFeS_2 Prepared by Mechanochemical Synthesis and Sintered by SPS. *Acta Phys. Pol. A* **2020**, *137*, 904–907. [[CrossRef](#)]
41. Wu, J.; Li, F.; Wei, T.R.; Ge, Z.H.; Kang, F.Y.; He, J.Q.; Li, J.F. Mechanical Alloying and Spark Plasma Sintering of BiCuSeO Oxyselenide: Synthesis Process and Thermoelectric Properties. *J. Am. Ceram. Soc.* **2016**, *99*, 507–514. [[CrossRef](#)]
42. Balaz, P.; Achimovicova, M.; Balaz, M.; Chen, K.; Dobrozhan, O.; Guilmeau, E.; Hejtmanek, J.; Knizek, K.; Kubickova, L.; Levinsky, P.; et al. Thermoelectric Cu-S-Based Materials Synthesized via a Scalable Mechanochemical Process. *ACS Sustain. Chem. Eng.* **2021**, *9*, 2003–2016. [[CrossRef](#)]

Disclaimer/Publisher’s Note: The statements, opinions and data contained in all publications are solely those of the individual author(s) and contributor(s) and not of MDPI and/or the editor(s). MDPI and/or the editor(s) disclaim responsibility for any injury to people or property resulting from any ideas, methods, instructions or products referred to in the content.